Longitudinal mode-coupling instabilities of proton bunches in the CERN Super Proton Synchrotron

Ivan Karpov[*]
CERN, CH-1211 Geneva, Switzerland

(Received 30 September 2022; accepted 19 December 2022; published 12 January 2023)

In this paper, we study single-bunch instabilities observed in the CERN Super Proton Synchrotron (SPS). According to the linearized Vlasov theory, radial or azimuthal mode-coupling instabilities result from a coupling of bunch-oscillation modes, which belong to either the same or adjacent azimuthal modes, respectively. We show that both instability mechanisms exist in the SPS by applying the Oide-Yokoya approach to compute van Kampen modes for the realistic longitudinal impedance model of the SPS. The results agree with macroparticle simulations and are consistent with beam measurements. In particular, we see that the uncontrolled longitudinal emittance blowup of single bunches observed before the recent impedance reduction campaign (2018–2021) is due to the radial mode-coupling instability. Unexpectedly, this instability is as strong as the azimuthal mode-coupling instability, which is possible in the SPS for other combinations of bunch length and intensity. We also demonstrate the significant role of rf nonlinearity and potential-well distortion in determining these instability thresholds. Finally, we discuss the effect of the recent impedance reduction campaign on beam stability in single- and double-rf configurations.

DOI: 10.1103/PhysRevAccelBeams.26.014401

I. INTRODUCTION

Longitudinal single-bunch instability is a possible performance limitation in many synchrotrons and its mechanism is the subject of various studies for a long time [1–16]. The standard approach to evaluate beam stability is based on a solution of the linearized Vlasov equation for a small initial perturbation of a stationary distribution function. To simplify the analysis, the modification of a stationary potential well by self-induced fields, called potential-well distortion (PWD), is often neglected. The only possible mechanism of longitudinal single-bunch instability with neither PWD nor multi-turn wakes, a coupling of different azimuthal modes, was proposed by Sacherer [1].

Another type of instability can be caused by asymmetry of the potential well due to PWD, resulting in a coupling of two radial modes within one azimuthal mode [8,9]. An explicit condition required for this instability to occur was found for the double-waterbag model [10]. For an impedance model consisting of one broadband resonator with frequency $f_r = \omega_r/2\pi$, the instability thresholds computed with and without PWD are similar for $\omega_r\sigma \gtrsim 0.4$, where σ is the rms bunch length, [8]. This result was also confirmed in calculations based on the orthogonal polynomial expansion [14]. The azimuthal mode coupling was also found in the self-consistent analysis of electron bunches for $\omega_r\sigma \approx \pi$ [13].

Similar to electron bunches, the thresholds of the single-bunch instability for proton bunches are often computed neglecting bunch asymmetry due to PWD and rf nonlinearity, as for example, in [11,17], and thus only azimuthal mode-coupling instability was found. To our best knowledge, for proton bunches, so far a radial mode-coupling instability was not observed in measurements nor in calculations.

In the SPS, the longitudinal instability of single proton bunches occurs during the acceleration ramp. The attempts to cure this instability by reducing the voltage in a single rf system and thus increasing the synchrotron frequency spread for a constant longitudinal emittance were not successful. Instead, a higher rf voltage was more beneficial [18]. In operation, this instability is cured by the application of a higher-harmonic (HH) rf system. Due to the strong frequency dependence of the SPS impedance [19,20] (Fig. 1), the observed instability was mainly studied in macroparticle simulations using the code BLonD [21]. The latest results of simulations through the ramp are consistent with measurements and the agreement has been improved with the refined impedance model [22].

In the present work, the mechanism of the SPS single-bunch instability is studied using code MELODY [23] which is able to find in a fully self-consistent way the numerical solutions of the matrix equations derived from the Vlasov equation for the full SPS impedance model. We show that

---

[*] ivan.karpov@cern.ch

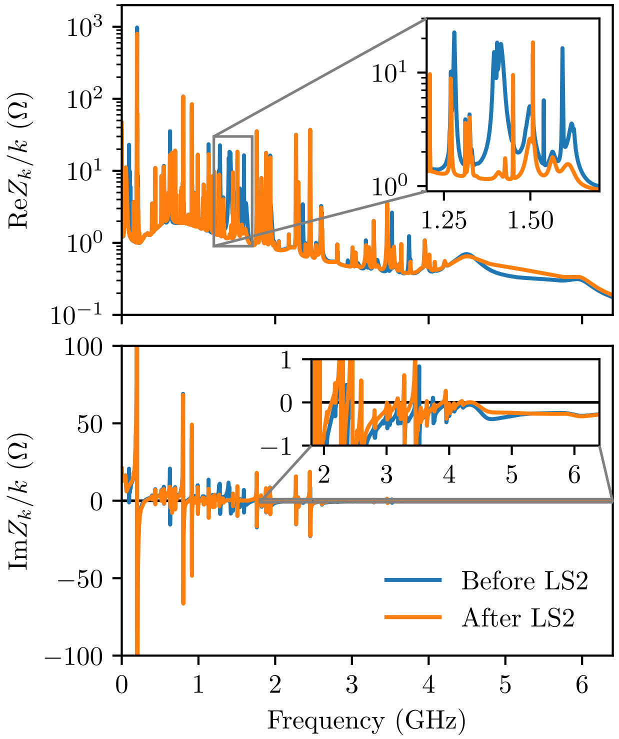

FIG. 1. SPS impedance model separated by real (top) and imaginary (bottom) parts before and after the impedance reduction campaign during the second Long Shutdown (LS2), which ended in March 2021.

the previously observed instability during the ramp was due to the coupling of multiple radial modes within one azimuthal mode. For a specific set of bunch parameters, we find an instability caused by the coupling of neighboring azimuthal modes for which Landau damping is lost. The main results are confirmed by macroparticle simulations with BLonD and are consistent with previous measurements [18].

The paper is organized as follows: In Sec. II, we briefly discuss the main definitions and numerical methods to evaluate single-bunch instabilities. Two possible instability mechanisms in the SPS and a comparison of calculations with measurements are presented in Sec. III. We consider different instability mitigation measures in Sec. IV and, finally, present the main conclusions.

II. MAIN EQUATIONS AND DEFINITIONS

The longitudinal motion of a particle in a synchrotron can be described in terms of its energy and phase deviations, ΔE and ϕ, relative to the synchronous particle with the energy E_0. For the efficient numerical implementation of beam stability analysis, it is convenient to introduce another set of variables, the energy $\mathcal{E}$ and the phase ψ of synchrotron oscillations

$$\mathcal{E} = \frac{\dot{\phi}^2}{2\omega_{s0}^2} + U_t(\phi), \tag{1}$$

$$\psi = \mathrm{sgn}(\eta\Delta E)\frac{\omega_s(\mathcal{E})}{\sqrt{2}\omega_{s0}}\int_{\phi_{\max}(\mathcal{E})}^{\phi}\frac{d\phi'}{\sqrt{\mathcal{E} - U_t(\phi')}}. \tag{2}$$

Here $\eta = 1/\gamma_{\mathrm{tr}}^2 - 1/\gamma^2$ is the phase slip factor, γ is the relativistic Lorentz factor, γ_{tr} is the Lorentz factor at transition energy, $f_{s0} = \omega_{s0}/2\pi$ is the frequency of small-amplitude synchrotron oscillations in a bare single-rf system, $\omega_s(\mathcal{E})$ is the synchrotron frequency as a function of $\mathcal{E}$, and $\phi_{\max}(\mathcal{E})$ is the maximum phase of the particle with synchrotron oscillation energy $\mathcal{E} = U_t[\phi_{\max}(\mathcal{E})]$. The total potential includes contributions from both the rf system and the beam-induced fields

$$U_t(\phi) = \frac{1}{V_1\cos\phi_{s0}}\int_{\Delta\phi_s}^{\varphi}[V_{\mathrm{rf}}(\phi') + V_{\mathrm{ind}}(\phi') - \delta E_0/q]d\phi', \tag{3}$$

where V_1 is the rf voltage amplitude of the main rf system, δE_0 is the energy gain per turn of the synchronous particle with charge q excluding intensity effects, $\Delta\phi_s$ is the synchronous phase shift due to intensity effects that satisfies the relation $\delta E_0/q = V_1\sin\phi_{s0} = V_{\mathrm{rf}}(\Delta\phi_s) + V_{\mathrm{ind}}(\Delta\phi_s)$, and ϕ_{s0} is the synchronous phase in a bare single-rf system. Below, we consider a double-rf system with a total voltage of

$$V_{\mathrm{rf}}(\phi) = V_1[\sin(\phi + \phi_{s0}) + r\sin(n\phi + n\phi_{s0} + \Phi_n)], \tag{4}$$

where Φ_n is the relative phase offset between the main and the HH rf systems with harmonic numbers h and nh, respectively, and $V_n = rV_1$ is the voltage amplitude of the HH rf system. For particular values of Φ_n, one can define two distinct regimes: bunch-shortening mode (BSM) when both rf systems are in phase at the bunch center and bunch-length mode (BLM) when both rf systems are in counterphase at the bunch center. In the SPS operation, they are chosen such that the contribution of the HH rf system is zero at $\phi = 0$ and it does not contribute to a shift of the synchronous phase. Thus, $\Phi_n = \pi - n\phi_{s0}$ for BSM and $\Phi_n = -n\phi_{s0}$ for BLM.

Note that the energy of the synchrotron oscillations, $\mathcal{E}$, is defined in units of the normalized rf potential, U_t, as can be seen from Eq. (3). The stationary rf bucket for the single-rf case without beam-induced fields is full when $\mathcal{E}_{\max} = 2$. In general, the total potential U_t depends on the particle distribution function, impedance model, and bunch intensity. It can be calculated using an iterative procedure [12,24]. In this work, we consider a particle distribution of the binomial family

$$\mathcal{F}(\mathcal{E}) = \frac{1}{2\pi\omega_{s0}A_N}\left(1-\frac{\mathcal{E}}{\mathcal{E}_{\max}}\right)^{\mu}, \tag{5}$$

with the normalization constant

$$A_N = \omega_{s0}\int_0^{\mathcal{E}_{\max}}\frac{d\mathcal{E}}{\omega_s(\mathcal{E})}\left(1-\frac{\mathcal{E}}{\mathcal{E}_{\max}}\right)^{\mu}. \tag{6}$$

For $\mu \to \infty$, the bunch has a Gaussian line density and the corresponding bunch length $\tau_{4\sigma}$ is typically defined as 4 times the rms bunch length σ, i.e., $\tau_{4\sigma} = 4\sigma$. The bunch length $\tau_{4\sigma}$ is related to the full width at half maximum (FWHM) bunch length τ_{FWHM} as $\tau_{4\sigma} = \tau_{\mathrm{FWHM}}\sqrt{2/\ln 2}$. In practice, SPS proton bunches are far from being Gaussian, and the best fit to the measured bunch profiles is for $\mu \approx 1.5$. This value will be assumed in the present work for all calculations and simulations. For easy comparison with measurements, we use

$$\tau_{\mathrm{eff}} = \tau_{\mathrm{FWHM}}\sqrt{2/\ln 2}, \tag{7}$$

as a definition of the effective bunch length. We also define the total longitudinal emittance in units of eVs as

$$\epsilon = \oint\frac{\Delta E(\phi)}{h\omega_0}d\phi = \sqrt{-\frac{V_1\cos\phi_{s0}\,q\beta^2E_0}{\pi\eta\omega_0^2h^3}}\epsilon_N, \tag{8}$$

with a dimensionless emittance

$$\epsilon_N = 2\int_{\phi_{\min}}^{\phi_{\max}}\sqrt{[\mathcal{E}_{\max} - U_t(\phi)]}d\phi, \tag{9}$$

where $\omega_0 = 2\pi f_0$ is the revolution frequency, $\phi_{\min}$ and $\phi_{\max}$ are the minimum and maximum phases of the particle with the energy of synchrotron oscillation $\mathcal{E}_{\max}$.

A. Linearized Vlasov equation

When the perturbation $\tilde{\mathcal{F}}$ to the stationary particle distribution function $\mathcal{F}(\mathcal{E})$ grows with time t, the beam is unstable. The initial time evolution of $\tilde{\mathcal{F}}$ is dictated by the linearized Vlasov equation (e.g., [25])

$$\frac{\partial\tilde{\mathcal{F}}}{\partial t} + \frac{d\mathcal{F}}{d\mathcal{E}}\frac{d\mathcal{E}}{dt} + \frac{\partial\tilde{\mathcal{F}}}{\partial\psi}\frac{d\psi}{dt} = 0. \tag{10}$$

After expansion over the azimuthal harmonics m of synchrotron motion, the solution of Eq. (10) at frequency Ω with the eigenfunctions $C_m(\mathcal{E},\Omega)$ [8]

$$\tilde{\mathcal{F}}(\mathcal{E},\psi,t) = e^{-i\Omega t}\sum_{m=1}^{\infty}C_m(\mathcal{E},\Omega)\left[\cos m\psi + \frac{i\Omega}{m\omega_s(\mathcal{E})}\sin m\psi\right] \tag{11}$$

leads to the integral equation

$$\begin{aligned}[\Omega^2 - m^2\omega_s^2(\mathcal{E})]C_m(\mathcal{E},\Omega) &= 2i\zeta\omega_{s0}^2\,m^2\omega_s^2(\mathcal{E})\frac{d\mathcal{F}(\mathcal{E})}{d\mathcal{E}}\sum_{m'=1}^{\infty}\int_0^{\mathcal{E}_{\max}}\frac{d\mathcal{E}'}{\omega_s(\mathcal{E}')}\\ &\times\sum_{k=-\infty}^{\infty}\frac{Z_k(\Omega)/k}{hZ_0}I_{mk}(\mathcal{E})I^*_{m'k}(\mathcal{E}')C_{m'}(\mathcal{E}',\Omega).\end{aligned} \tag{12}$$

Here $Z_k(\Omega) = Z(k\omega_0 + \Omega)$ is the longitudinal impedance at frequency $k\omega_0 + \Omega$ and $Z_0 \approx 377\ \Omega$ is the impedance of free space. We also introduced the dimensionless intensity parameter

$$\zeta = -\frac{qN_ph^2\omega_0Z_0}{V_1\cos\phi_{s0}}, \tag{13}$$

with N_p being the bunch intensity. The function $I_{mk}(\mathcal{E})$ is defined as

$$I_{mk}(\mathcal{E}) = \frac{1}{\pi}\int_0^{\pi}e^{ik\phi(\mathcal{E},\psi)/h}\cos m\psi\,d\psi. \tag{14}$$

Detailed derivations of Eq. (12) using variables $(\mathcal{E},\psi)$ can be found in [26] and it is identical to Eq. (41) therein. For a given impedance model, the single-bunch stability depends on the two dimensionless parameters, ζ and ϵ_N, as well as on the parameters of the rf potential: n, ϕ_{s0}, r, and Φ_n. This fact will be applied below to understand the mechanisms of instabilities observed in the SPS.

B. van Kampen modes

The integral equation (12) is equivalent to the equation that describes collective modes in a plasma [27–29]. An initial perturbation can be expressed as a superposition of van Kampen modes, which are, in general, described by nonregular functions. In the early 80s, the concept of van Kampen modes was introduced by Chin *et al.* to describe bunch oscillations [4]. Additionally, the general expression for these modes was derived. Here, we revisit this expression of van Kampen modes to highlight the specificity of stable and unstable modes.

First, one can perform the substitution in Eq. (12)

$$C_m(\mathcal{E},\Omega) = \sqrt{-\omega_s(\mathcal{E})\frac{d\mathcal{F}(\mathcal{E})}{d\mathcal{E}}}m\frac{\omega_s(\mathcal{E})}{\omega_{s0}^2}\tilde{C}_m(\mathcal{E},\Omega), \tag{15}$$

which leads to

$$\left[\frac{\Omega^2}{\omega_{s0}^2} - \frac{m^2\omega_s^2(\mathcal{E})}{\omega_{s0}^2}\right]\tilde{C}_m(\mathcal{E},\Omega) = -2i\zeta\sum_{m'=1}^{\infty}\int_0^{\mathcal{E}_{\max}}K_{mm'}(\mathcal{E},\mathcal{E}')\tilde{C}_{m'}(\mathcal{E}',\Omega)d\mathcal{E}'. \tag{16}$$

Here, the kernel K is defined as

$$K_{mm'}(\mathcal{E},\mathcal{E}',\Omega) = \sum_{k=-\infty}^{\infty} \frac{Z_k(\Omega)/k}{hZ_0} \times m\sqrt{-\omega_s(\mathcal{E})\frac{d\mathcal{F}(\mathcal{E})}{d\mathcal{E}}} I_{mk}(\mathcal{E}) \times m'\sqrt{-\omega_s(\mathcal{E}')\frac{d\mathcal{F}(\mathcal{E}')}{d\mathcal{E}'}} I^*_{m'k}(\mathcal{E}'). \tag{17}$$

Then, introducing a set of orthonormal functions $s_n^{(m)}$,

$$\int_0^{\mathcal{E}_{\max}} s_n^{(m)}(\mathcal{E}) s_{n'}^{(m)}(\mathcal{E}) d\mathcal{E} = \delta_{nn'},$$

with the Kronecker delta δ_{ij}, we can decompose $\tilde{C}_m$ and $K_{mm'}$, similarly to [4]:

$$\tilde{C}_m(\mathcal{E},\Omega) = \sum_{n=0}^{\infty} a_m^n(\Omega) s_n^{(m)}(\mathcal{E}), \tag{18}$$

$$K_{mm'}(\mathcal{E},\mathcal{E}',\Omega) = \sum_{n=0}^{\infty}\sum_{n'=0}^{\infty} K_{mm'}^{nn'} s_n^{(m)}(\mathcal{E}) s_{n'}^{(m')}(\mathcal{E}'), \tag{19}$$

with the coefficients a_m^n and $K_{mm'}^{nn'}$ defined as

$$a_m^n(\Omega) = \int_0^{\mathcal{E}_{\max}} \tilde{C}_m(\mathcal{E},\Omega) s_n^{(m)}(\mathcal{E}) d\mathcal{E}, \tag{20}$$

and

$$K_{mm'}^{nn'}(\Omega) = \int_0^{\mathcal{E}_{\max}}\int_0^{\mathcal{E}_{\max}} K_{mm'}(\mathcal{E},\mathcal{E}',\Omega) s_n^{(m)}(\mathcal{E}) \times s_{n'}^{(m')}(\mathcal{E}') d\mathcal{E} d\mathcal{E}', \tag{21}$$

respectively. The examples of the orthogonal functions which can be used in practice will be discussed in Sec. II D. Finally, inserting Eqs. (18) and (19) in Eq. (16), we obtain the eigenfunctions, i.e., the general expression for van Kampen modes

$$\tilde{C}_m(\mathcal{E},\Omega) = -\left\{ \mathrm{P}\frac{1}{\Omega^2 - m^2\omega_s^2(\mathcal{E})} + \alpha(\mathcal{E},\Omega)\delta[\Omega^2 - m^2\omega_s^2(\mathcal{E})] \right\} \times 2i\zeta\omega_{s0}^2 \sum_{m'=1}^{\infty}\sum_{n=0}^{\infty}\sum_{n'=0}^{\infty} K_{mm'}^{nn'}(\Omega) a_{m'}^{n'}(\Omega) s_n^{(m)}(\mathcal{E}), \tag{22}$$

where P denotes the principal value of the integral, and $\alpha(\mathcal{E},\Omega)$ can be found from the normalization condition

$$\sum_{m=1}^{\infty}\int_0^{\mathcal{E}_{\max}} \tilde{C}_m(\mathcal{E},\Omega) d\mathcal{E} = 1.$$

For $\mathrm{Im}\Omega \to \pm 0$, for example, one gets $\alpha = \mp i\pi$.

Most of the stable modes are located within the incoherent spectrum $\Omega \in m\omega_s(\mathcal{E})$ and have singular eigenfunctions due to the second term in braces in Eq. (22). Unstable modes and modes for which Landau damping is lost, $\Omega \notin m\omega_s(\mathcal{E})$, have regular eigenfunctions as they are defined by the first terms in braces.

C. Instability mechanisms

The eigenfunctions are related to the perturbed line density harmonics (see, e.g., in [26])

$$\tilde{\lambda}_k(\Omega) = \frac{\omega_{s0}^2}{h}\sum_{m=1}^{\infty}\int_0^{\mathcal{E}_{\max}} \frac{C_m(\mathcal{E},\Omega) I^*_{mk}(\mathcal{E})}{\omega_s(\mathcal{E})} d\mathcal{E}. \tag{23}$$

Multiplying Eq. (16) with $\tilde{C}_m^*(\mathcal{E},\Omega)$, integrating over $\mathcal{E}$, and summing over m leads to

$$\Omega^2 = \sum_{m=1}^{\infty}\int_0^{\mathcal{E}_{\max}} m^2\omega_s^2(\mathcal{E}) \frac{|\tilde{C}_m(\mathcal{E},\Omega)|^2}{B(\Omega)} d\mathcal{E} + \frac{2\zeta h\omega_{s0}^2}{B(\Omega)} \sum_{k=-\infty}^{\infty} \frac{\mathrm{Im}Z_k(\Omega)/k}{Z_0} |\tilde{\lambda}_k(\Omega)|^2 - \frac{2i\zeta h\omega_{s0}^2}{B(\Omega)} \sum_{k=-\infty}^{\infty} \frac{\mathrm{Re}Z_k(\Omega)/k}{Z_0} |\tilde{\lambda}_k(\Omega)|^2, \tag{24}$$

where

$$B(\Omega) = \sum_{m=1}^{\infty}\int_0^{\mathcal{E}_{\max}} |\tilde{C}_m(\mathcal{E},\Omega)|^2 d\mathcal{E}.$$

Below the instability threshold, i.e., $\mathrm{Im}\Omega = 0$, the contribution of the last term in Eq. (24) must be zero as it is purely imaginary. Depending on the sign of the sum on the second line of Eq. (24), the mode frequency can be shifted upwards or downwards with respect to the weighted incoherent frequency, i.e., first line of Eq. (24). Thus, two modes those frequencies approach each other can couple leading to mode-coupling instability. In some cases, one can distinguish two types of instabilities: radial and azimuthal mode coupling. The former usually appears when different azimuthal modes are well separated as a result of a small synchrotron frequency spread and two coupled modes belong to the same azimuthal mode. The latter mechanism requires a significant frequency shift of the modes as well as a significant synchrotron frequency spread, so the modes with different azimuthal mode numbers can couple. Both instability types can be found using self-consistent analysis. Neglecting PWD and rf nonlinearity, only the classical azimuthal mode-coupling instability [1] is possible (see Appendix).

The above-mentioned mode-coupling instabilities can be driven by broadband resonator impedance sources, for example. In the presence of the multiturn wakes, Robinson-type instabilities can potentially exist. However, the characteristic damping times $2Q_r/\omega_r$ with Q_r being the quality factor of the resonator impedance are significantly shorter than the revolution period for all known elements of the SPS impedance model. Also, the resistive-wall wake of the SPS decays by more than 5 orders of magnitude after one turn due to a large SPS circumference. Thus, the Robinson-type instability is excluded from the analysis in this paper.

In the case of instability, we obtain the growth rate from Eq. (24)

$$\mathrm{Im}\Omega = -\frac{\zeta h \omega_{s0}^2}{B(\Omega)\mathrm{Re}\Omega}\sum_{k=-\infty}^{\infty}\frac{\mathrm{Re}Z_k(\Omega)/k}{Z_0}|\tilde{\lambda}_k(\Omega)|^2, \qquad (25)$$

which shows that for a smooth impedance, $Z_{-k}(\Omega) \approx Z_k^*(\Omega)$, at least for some harmonics of the revolution frequency, k, the power spectral harmonics must differ

$$|\tilde{\lambda}_{-k}(\Omega)|^2 \neq |\tilde{\lambda}_k(\Omega)|^2.$$

A similar conclusion was obtained in [13], pointing out the possibility of radial mode-coupling instability within a single azimuthal mode in the presence of PWD. Equation (25) shows, however, that the asymmetry of the mode spectrum is the general property of unstable modes, irrespective of the single-bunch instability mechanism.

Below, we will discuss the methods of computing the van Kampen modes for cases of practical applications.

D. Methods to solve the linearized Vlasov equation

To solve the integral equation (12), it is usually converted to the infinite system of equations

$$\frac{\Omega^2}{\omega_{s0}^2}a_m^n(\Omega) = \sum_{n'=0}^{\infty}\sum_{m'=1}^{\infty}M_{mm'}^{nn'}(\Omega)a_{m'}^{n'}(\Omega), \qquad (26)$$

where the matrix elements are defined as (see, e.g., [2,4])

$$M_{mm'}^{nn'}(\Omega) = m^2\delta_{mm'}\int_0^{\mathcal{E}_{\max}}\frac{\omega_s^2(\mathcal{E})}{\omega_{s0}^2}s_n^{(m)}(\mathcal{E})s_{n'}^{(m)}(\mathcal{E})d\mathcal{E} - 2i\zeta K_{mm'}^{nn'}(\Omega). \qquad (27)$$

The system of equations (26) becomes linear if the dependence of the matrix elements $M_{mm'}^{nn'}$ on Ω can be neglected. This requires a rather smooth dependence of impedance on the frequency, so that $Z_k(\Omega) \approx Z_k(0)$, which is valid for the SPS impedance where the bandwidth of all relevant resonant peaks is larger than the revolution frequency f_0. Then, after truncation of the infinite sums over indices m, n, and k, Eq. (26) can be solved as a standard eigenvalue problem.

Two methods exist to compute the matrix elements depending on the choice of the orthonormal functions: the orthogonal polynomial expansion [2] and the Oide-Yokoya method [8]. For the former method, the orthonormal functions for a particle distribution according to Eq. (5) can be constructed from the Jacobi polynomials $P_n^{(\alpha,\beta)}(x)$,

$$s_n^{(m)}(\mathcal{E}) = \sqrt{\frac{(2n+m+\mu)\Gamma(n+1)\Gamma(n+m+\mu)}{\Gamma(n+m+1)\Gamma(n+\mu)}} \times\sqrt{-\frac{2\pi\omega_{s0}A_N}{\mu}\frac{d\mathcal{F}(\mathcal{E})}{d\mathcal{E}}}\left(\frac{\mathcal{E}}{\mathcal{E}_{\max}}\right)^{m/2} \times P_n^{(m,\mu-1)}\left(1-\frac{2\mathcal{E}}{\mathcal{E}_{\max}}\right), \qquad (28)$$

where n is the radial mode number and $\Gamma(x)$ is the Gamma function. For the latter approach, steplike functions [8] are used

$$s_n^{(m)}(\mathcal{E}) = \begin{cases}\frac{1}{\sqrt{\Delta\mathcal{E}_n}}, & \mathcal{E}_n - \frac{\Delta\mathcal{E}_n}{2} < \mathcal{E} \leq \mathcal{E}_n + \frac{\Delta\mathcal{E}_n}{2}\\ 0, & \text{elsewhere,}\end{cases}$$

where $\mathcal{E}_n$ is the nth mesh point on the energy grid, and $\Delta\mathcal{E}_n$ is the thickness of the corresponding strip. Additionally, integrals in Eq. (21) are approximated by sums, so $K_{mm'}^{nn'}(\Omega) \approx \sqrt{\Delta\mathcal{E}_n\Delta\mathcal{E}_{n'}}K_{mm'}(\mathcal{E}_n,\mathcal{E}_{n'},\Omega)$ and the matrix elements of the eigenvalue problem (26) become

$$M_{mm'}^{nn'}(\Omega) = \frac{m^2\omega_s^2(\mathcal{E}_n)}{\omega_{s0}^2}\delta_{nn'}\delta_{mm'} - 2i\zeta\sqrt{\Delta\mathcal{E}_n\Delta\mathcal{E}_{n'}}K_{mm'}(\mathcal{E}_n,\mathcal{E}_{n'},\Omega). \qquad (29)$$

Both methods to solve the linearized Vlasov equation are implemented in the MELODY code and allow the evaluation of single-bunch stability for arbitrary impedance models. As the first step, the stationary potential U_t is found using an iterative procedure [12,24,26]. Then, 2D arrays of functions $I_{mk}(\mathcal{E})$ are computed for grid points in $\mathcal{E}$ and k for different azimuthal modes m. The "continuous" functions are constructed from these arrays using a cubic spline interpolation to evaluate the matrix elements $M_{mm'}^{nn'}$. Finally, the eigenvalue problem is solved. We find that the Oide-Yokoya method has better convergence properties than the orthogonal polynomial expansion. This is thanks to a nonuniform mesh with respect to the energy of synchrotron oscillations $\mathcal{E}_n$, which allows for improved resolution around "critical" points. For example, in the case of instability with $\mathrm{Re}\Omega = m\omega_s(\tilde{\mathcal{E}})$, one can expect a resonance with a characteristic width of

$$\delta\mathcal{E} \approx \left| \mathrm{Im}\Omega/m \frac{d\omega_s(\mathcal{E})}{d\mathcal{E}} \bigg|_{\mathcal{E}=\tilde{\mathcal{E}}} \right|.$$

If $\delta\mathcal{E} \ll \mathcal{E}_{\max}$, a very high-resolution mesh in $\mathcal{E}$ might be needed to find a converged solution.

III. LONGITUDINAL SINGLE-BUNCH INSTABILITIES IN THE SPS

In this section, we will show first the results of stability analysis at the SPS flattop (450 GeV) and then through acceleration. The SPS has a double-rf system with frequencies of 200 and 800 MHz ($n = 4$). The main accelerator and beam parameters are listed in Table I. Here, we will discuss a single-rf operation, while stability in a double-rf case will be addressed in Sec. IV.

It has been shown in previous studies that in a single-rf operation, the single-bunch intensity threshold is a noncontinuous and nonmonotonic function of the bunch length [18,31]. Since then, the SPS impedance model has been further refined, and below, we will show the simulation results based on this latest model (Fig. 1).

The beam stability in simulations is probed by observing the growing oscillations of the bunch position (dipole) and length (quadrupole). The instability can emerge from the initial seed and can be detected during a finite simulation time for a sufficiently large instability growth rate. In Fig. 2, we show a stability map obtained from a scan in bunch intensity N_p (in steps of 2.5×10^{10}) and bunch length τ_{eff} (in steps of 50 ps) in simulations for 10^6 macroparticles. For each pair (N_p, τ_{eff}) a bunch is generated initially matched to the total potential U_t including intensity effects so that the longitudinal emittance is found iteratively assuming constant rf parameters and the distribution type (5). The impedance model before the second long shutdown (LS2) shown in Fig. 1 was taken. In simulations, the maximum amplitude of the bunch-length oscillations $\Delta\tau_{\mathrm{eff}}$ divided by the average bunch length τ_{eff} during 10^5 turns (about 600 synchrotron periods) indicates the bunch stability [32].

The numerical results calculated using code MELODY with up to ten azimuthal modes are shown in Fig. 3. This number of azimuthal modes was sufficient to obtain converged results. The scan was performed on a grid of $(\mathcal{E}, \zeta)$ values. The bunch length τ_{eff} and intensity N_p values were computed for each pair of parameters and then used to create an interpolated map of the corresponding growth rates. The impedance model is truncated at $k_{\max} f_0 \approx 6.4$ GHz, while the radial mesh is automatically refined depending on the bunch length (in some cases up to $N_{\mathcal{E}} \approx 10^3$ mesh points in the energy of synchrotron oscillations).

TABLE I. The SPS parameters at the flattop energy [30].

Parameter	Units	Value
Circumference, C	m	6911.554
Beam energy, E_0	GeV	450
Transition Lorentz factor, γ_{tr}		17.951
Main harmonic number, h		4620
Main rf frequency, f_{rf}	MHz	200.394
Main rf voltage amplitude, V_1	MV	7.2

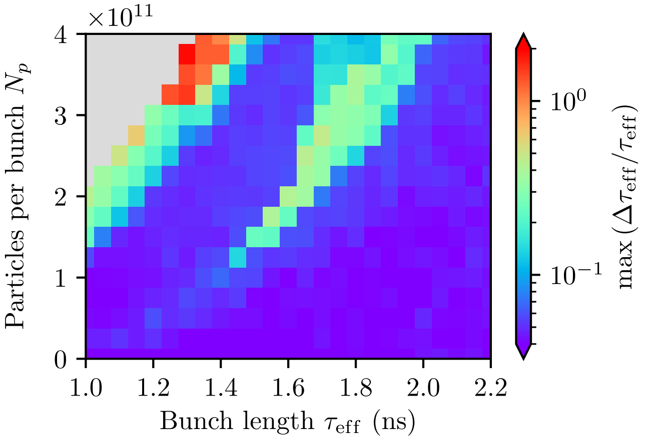

FIG. 2. Longitudinal stability map obtained from BLonD simulations for single-rf operation ($r = 0$) and with the pre-LS2 impedance model (Fig. 1). The color code indicates the maximum relative oscillation amplitude of the bunch length during 10^5 turns. The gray area indicates parameters for which the initial stationary distribution was not found. The SPS parameters are according to Table I.

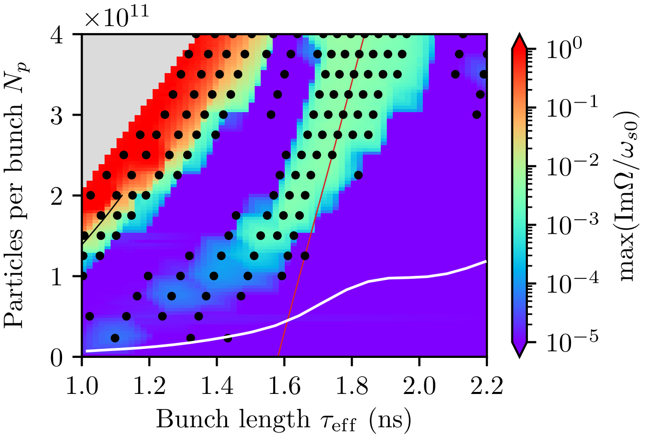

FIG. 3. Longitudinal stability map obtained from calculations with code MELODY (bottom) for the same parameters as in Fig 2. The color code shows the growth rate of the most unstable mode, while the gray area indicates parameters for which stationary distribution was not found. The bunch parameters for which synchrotron frequency is a nonmonotonic function of $\mathcal{E}$ are shown as black circles. The black and red lines show examples of the bunch-length dependence on intensity due to PWD for constant energy of synchrotron oscillations $\mathcal{E}_{\max} = 0.12$ and $\mathcal{E}_{\max} = 0.57$, respectively. The solid white curve corresponds to the LLD threshold computed with MELODY.

In general, one can see that the stable solutions (purple) correspond to BLonD simulations where bunch length stays constant (the oscillation amplitude is below the noise level $\Delta\tau_{\mathrm{eff}}/\tau_{\mathrm{eff}} < 0.04$), while τ_{eff} grows for most of the unstable solutions with nonnegligible growth rates. Both methods show that there is an unstable "island" approximately for intensities above 1.5×10^{11} and the bunch length in the range of 1.5–1.9 ns.

In addition, in Fig. 3, the circles indicate the cases with a nonmonotonic behavior of the synchrotron frequency as a function of the energy of synchrotron oscillations. In the past, it was shown that coupling of radial modes within a single azimuthal can occur in this case [9]. We observe that the instability often is correlated with the presence of $d\omega_s/d\mathcal{E} = 0$ inside the bunch, however, it is not always the case. This can be understood from the fact that for a particular set of bunch parameters, the growth rate can be very small, and it is difficult to detect in simulations or to properly resolve in numerical calculations. Still, the nonmonotonic behavior of the synchrotron frequency distribution could be a useful indication that we can expect instability.

We also show in Fig. 3 with a solid white line, the threshold of loss of Landau damping (LLD) computed numerically with MELODY for a dipole mode ($m = 1$) in the same way as in [26]. Alternatively, it can be also evaluated analytically by applying a concept of the effective impedance and effective cutoff frequency [26,33], which for the SPS impedance model before LS2 are about 2 Ω and 1.4 GHz, respectively. The LLD threshold is a monotonic function, thus it increases for a larger bunch length. However, the actual instability threshold is significantly higher. Even though Landau damping is already lost and the coherent modes are outside the incoherent band, their amplitudes do not grow in simulations without external noise. In operation, the excitation of these modes, for example, due to some noise in the rf system, is suppressed by the phase loop. Thus, we conclude that LLD does not trigger the observed instability of a single bunch in the SPS. Two other instability mechanisms will be discussed in the following subsection.

A. Radial mode-coupling instability

To clarify the instability mechanism inside an unstable "island," we plot van Kampen modes as a function of intensity for constant energy of synchrotron oscillations $\mathcal{E}_{\max} = 0.57$ (beam parameters according to the red line in Fig. 3) in Fig. 4. The real part of the first six azimuthal modes (top plot) does not overlap for the entire intensity range. It means that only coupling of radial modes of the same azimuthal mode is possible for these parameters. The lowest threshold intensity is for the third azimuthal mode (green curve on the bottom plot of Fig. 4), while for higher intensity other azimuthal modes are also unstable. In that case, we can observe "microwave-like" instability as the bunch line density will be modulated by a mixture of several unstable modes.

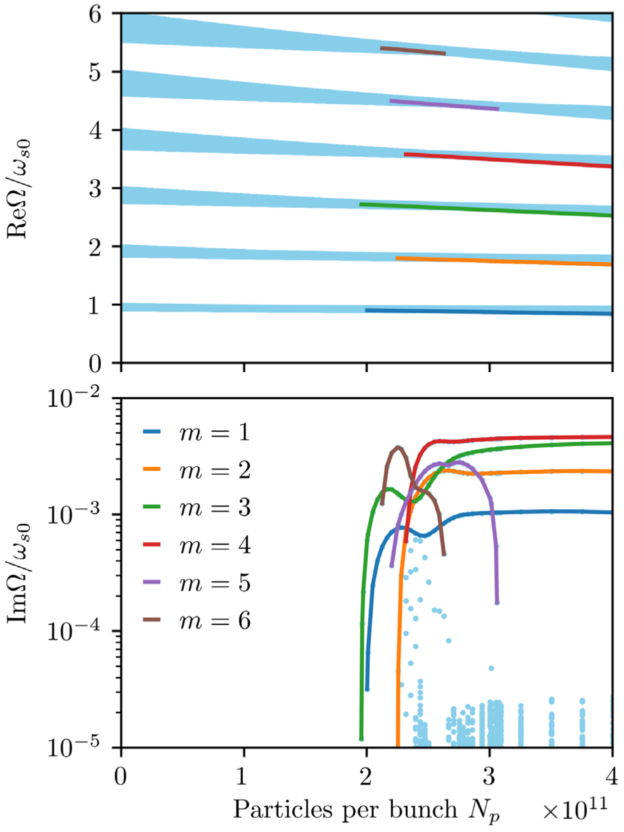

FIG. 4. Real (sorted and joined by light blue lines, top) and imaginary (blue dots, bottom) parts of van Kampen modes as functions of bunch intensity for $\mathcal{E}_{\max} = 0.57$. Unstable modes of the first six azimuthal modes are plotted as colored lines. Beam parameters correspond to those indicated by the red line in Fig. 3.

The synchrotron frequency distribution inside the unstable "island" is strongly affected by PWD and the initial rf nonlinearity plays an important role (see Fig. 5). At the threshold of instability (orange curve), $d\omega(\mathcal{E})/d\mathcal{E}$ approaches zero and at the same time $d^2\omega(\mathcal{E})/d\mathcal{E}^2 = 0$. This shape can be achieved for double-rf operation in BSM for $n > 2$, while here it is a result of PWD. For even higher intensity, the overlap of synchrotron frequencies for different $\mathcal{E}$ values becomes more significant.

In this example, instability occurs due to the coupling of two modes inside the incoherent synchrotron frequency spread. The unstable modes of the first four azimuthal modes move below the minimum incoherent frequency and remain unstable for higher intensities. The instability of higher-order azimuthal modes is suppressed above a certain intensity. For example, a zoomed region around the fifth azimuthal mode is shown in Fig. 6. At the intensity of about 3.1×10^{11} the modes are again decoupled, which results in suppression of this instability.

For completeness, the results of analysis when rf nonlinearity and PWD are neglected are also performed for the

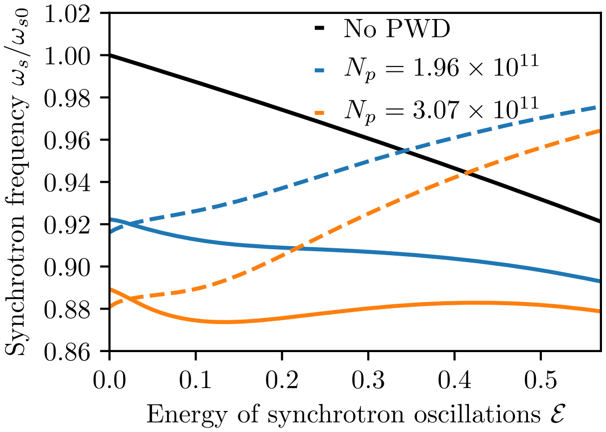

FIG. 5. Synchrotron frequency as a function of synchrotron-oscillation energy for different intensities and $\mathcal{E}_{\max} = 0.57$. Solid lines are for single-rf potential, while dashed lines are for a parabolic-rf potential. The black curve illustrates the case without PWD.

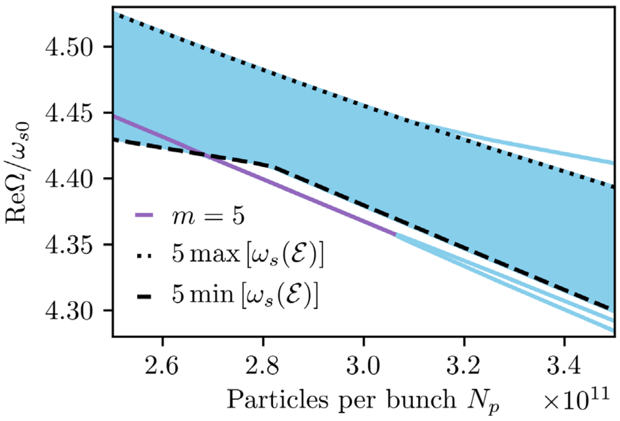

FIG. 6. Zoomed version of Fig. 4 (top plot). Blue lines represent van Kampen modes, while the unstable mode is shown in purple. The minimum and maximum incoherent synchrotron frequencies of the fifth azimuthal mode are plotted as dashed and dotted lines, respectively.

same $\mathcal{E}_{\max} = 0.57$. As discussed in Sec. II C, only azimuthal mode-coupling instability is possible in this case. Its threshold is almost a factor of 5 higher than the one obtained in self-consistent calculations (Fig. 7). It means that the self-consistent analysis is crucial to predict the instability threshold for relatively long bunches.

B. Azimuthal mode-coupling instability

A different mechanism of instability can be observed for shorter bunches. Figure 8 shows the real part of van Kampen modes of quadrupole and sextupole azimuthal modes as a function of intensity for $\mathcal{E}_{\max} = 0.12$ (black curve in Fig. 3). One can see a quadrupole mode for which Landau damping is lost. It is moving toward the frequency band of radial modes with azimuthal mode number $m = 3$. At the same time, a sextupole mode of LLD type moves down toward the radial modes with $m = 2$ (Fig. 9). This mode could emerge due to a strong PWD, which leads to

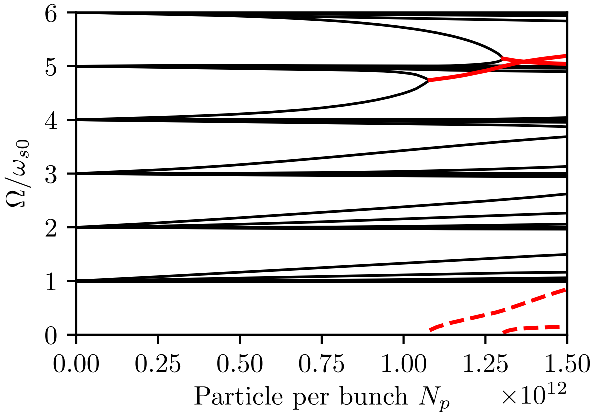

FIG. 7. Real (solid lines) and imaginary (dashed lines) parts of van Kampen modes as functions of bunch intensity for $\mathcal{E}_{\max} = 0.57$, neglecting rf nonlinearity and PWD.

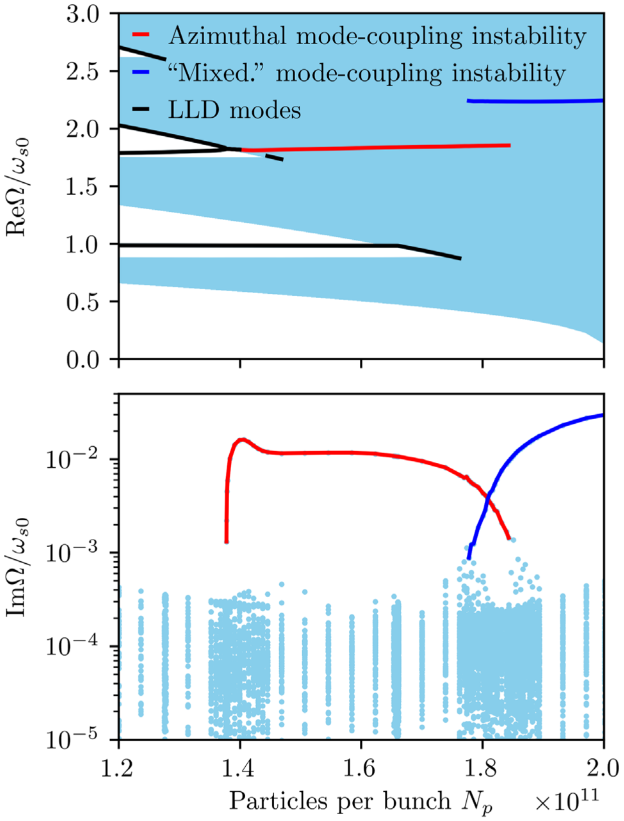

FIG. 8. Real (sorted and joined by light blue lines, top) and imaginary (blue dots, bottom) as functions of bunch intensity for $\mathcal{E}_{\max} = 0.12$ (bunch parameters correspond to those indicated by the black line in Fig. 3). Black lines show the frequencies of the mode for which Landau damping is lost. The red and blue lines indicate the unstable modes.

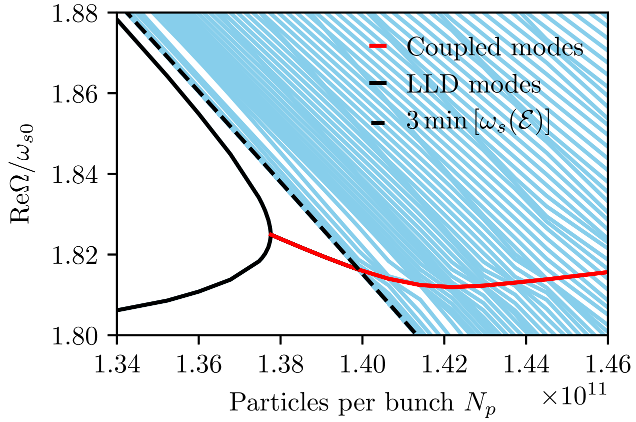

FIG. 9. Zoomed version of the top plot in Fig. 8 demonstrating the coupling of quadrupole and sextupole modes. The dashed line is the minimum incoherent synchrotron frequency of the third azimuthal mode.

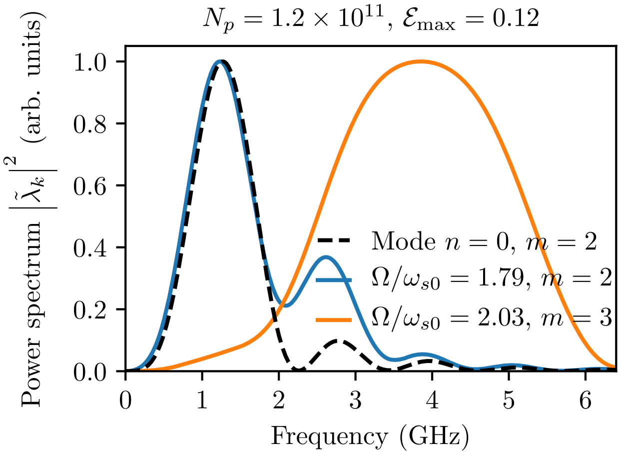

FIG. 11. Power spectra of quadrupole (blue) and sextupole (orange) azimuthal modes of the LLD type. The dashed line corresponds to the zeroth radial mode of the quadrupole azimuthal mode evaluated using Eqs. (23) and (28).

the formation of a local minimum of the synchrotron frequency as a function of the synchrotron oscillation energy (blue curve in Fig. 10). Note also that rf nonlinearity does not play a significant role, as itself it results in a synchrotron frequency spread that is negligible in comparison to the one created by PWD (black curve in Fig. 10). At the intensity of 1.37×10^{11}, those two modes are coupled and thus result in azimuthal mode-coupling instability. The growth rate of the instability increases while the coupled modes remain outside the incoherent frequency bands ($N_p \lesssim 1.4 \times 10^{11}$). Then, the growth rate is slightly suppressed and weakly depends on intensity once the coupled modes move inside the sextupole synchrotron frequency band. This is very different from the azimuthal-mode coupling instability predicted by Sacherer [1] for which the growth rate is a strong function of intensity. Since this instability involves the LLD mode of the sextupole synchrotron frequency band, which emerges below the minimum synchrotron frequency, it is very sensitive to particle distribution. As the distribution modifies after the start of the instability, the modes can be decoupled again leading to beam stabilization.

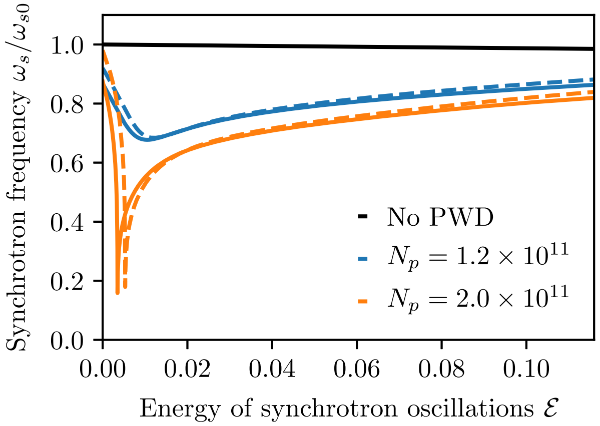

FIG. 10. Synchrotron frequency as a function of synchrotron-oscillation energy for different intensities and $\mathcal{E}_{\max} = 0.12$. Solid lines are for single-rf potential, while dashed lines are for a parabolic-rf potential (linear rf voltage). The black curve illustrates the case without PWD.

Equation (24) can be applied to understand why these modes move in different directions as a function of intensity. Figure 11 shows that the power spectrum of the quadrupole mode (blue curve) has a larger overlap with positive values of $\mathrm{Im}Z_k/k$ (Fig. 1). Thus, its frequency shift will be positive as the cumulative sum $\sum_k \mathrm{Im}Z_k/k|\tilde{\lambda}_k|^2$ is positive. The opposite situation is true for the LLD mode with $m = 3$, for which the maximum power spectrum is localized at the higher frequencies where $\mathrm{Im}Z_k/k$ is mostly negative. In this case, the mode is moving downwards in frequency as the intensity increases.

We also find that the LLD mode above the maximum incoherent frequency of the second azimuthal mode is dominated by the zeroth radial mode (dashed curve in Fig. 11), which is defined by Eqs. (23) and (28). On the contrary, the LLD mode below the third azimuthal mode is actually a superposition of a few hundred radial modes, which makes it more difficult to find a converging solution using the orthogonal polynomial expansion. To see this precisely, the computed expansion coefficients a_m^n from Eqs. (20) and (28) are shown in Fig. 12.

There are no LLD modes above maximum incoherent frequency for $m > 2$. This can be understood from the fact that their power spectra are localized at higher frequencies, and the modes sample mostly the negative values of $\mathrm{Im}Z_k/k$. Thus, the modes are pushed inside the incoherent frequency band and remain Landau-damped.

Although the threshold of azimuthal mode-coupling instability is clearly defined ($N_p \approx 1.37 \times 10^{11}$), one can

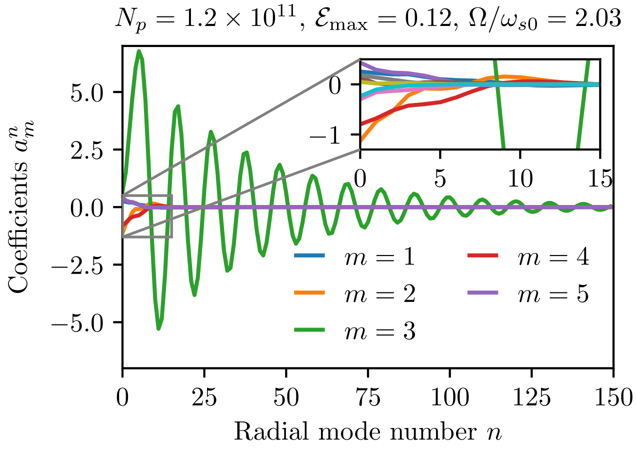

FIG. 12. Coefficients of the orthogonal polynomial expansion according to Eq. (20) for the LLD mode shown as an orange curve in Fig. 11.

observe the modes with growth rates $\mathrm{Im}\Omega/\omega_{s0} \sim 10^{-4}$ for lower intensities. In this case, $\omega_s(\mathcal{E})$ has a local minimum (Fig. 10) and, therefore, radial mode-coupling instability can appear. However, these unstable modes are localized at small values of $\mathcal{E}$, which makes it difficult to find converged solutions as was discussed in Sec. II D. Additionally, the spectra of these modes are localized at high frequencies and they sample a rather small residual part of the real impedance (Fig. 1), which supports expectations of very small growth rates.

Above a certain intensity of about $\sim 1.8 \times 10^{11}$, we also observe another unstable mode (blue curve in Fig. 8). It involves van Kampen modes, which are inside the synchrotron frequency spread leading to the radial mode-coupling instability. However, a strong PWD leads to an overlap of several azimuthal synchrotron frequency bands as the minimum synchrotron frequency is rather low (Fig. 10). The eigenvector of the unstable mode has resonant behavior for several azimuthal modes where $m\omega_s(\mathcal{E}) = \mathrm{Re}\Omega$, which can be seen in the longitudinal phase space (Fig. 13). This can be called a "mixed" mode-coupling instability, which has features of both radial and azimuthal mode-coupling instabilities. For even higher intensities, the PWD leads to the formation of the second local minimum of the potential well and the minimum synchrotron frequency approaches zero. In that case, there are two distinct branches for the possible solutions that start from two different fixed points [8,14]. In our calculations, we show the results for the branch with the lowest minimum of the potential well and, in most cases, we observe an extremely fast instability with a growth time of a few synchrotron periods. Since the synchrotron frequency bands for different azimuthal modes significantly overlap, it is difficult to distinguish which modes are coupled for a particular set of bunch parameters.

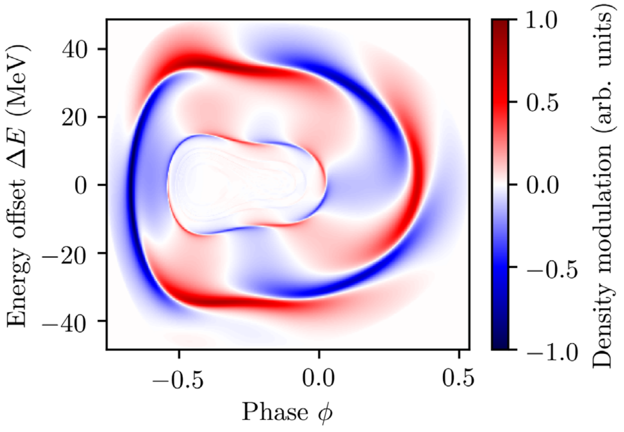

FIG. 13. Phase space of the most unstable mode for $N_p = 2.0 \times 10^{11}$ and $\mathcal{E}_{\max} = 0.12$ computed with MELODY using the SPS impedance model from before LS2. The SPS parameters are according to Table I.

Figure 14 shows the results of calculations where rf nonlinearity and PWD are neglected, similar to Fig. 7 in the previous subsection. In that case, we again find the coupling of the quadrupole and sextupole azimuthal modes, while the instability threshold is about 25% higher in comparison to the results of the self-consistent analysis. A similar dependence of the mode frequencies as a function of intensity can be achieved by using a single broadband resonator impedance model with the resonant frequency at about 1.4 GHz. Since the zero-intensity bunch length is $\tau_{\mathrm{eff}} \approx 0.75$ ns, we get $\omega_r\sigma \approx 1.7$. As was shown in the original work of Oide and Yokoya [8], the results of self-consistent calculations are close to those obtained neglecting PWD and rf nonlinearity $\omega_r\sigma > 0.4$.

In the recent publication [17], the instability analysis was performed for the SPS parameters and the azimuthal mode-coupling instability was found assuming a single broadband resonator impedance with a resonant frequency of 1 GHz. Additionally, a 10 times smaller rf frequency

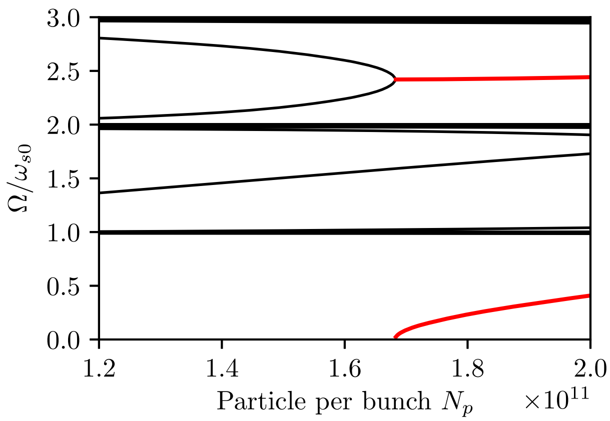

FIG. 14. Real (solid lines) and imaginary (dashed lines) parts of van Kampen modes as functions of bunch intensity for $\mathcal{E}_{\max} = 0.12$, when rf nonlinearity and PWD are neglected.

compared to the actual rf frequency was used to exclude the contribution of rf nonlinearity. The computed instability threshold was slightly higher than the one obtained in simulations. Our self-consistent analysis, instead, finds the radial mode-coupling instability. Since $\omega_r \sigma \approx 4.3$, two types of numerical calculations give similar results as expected. Nevertheless, the growth rates as a function of intensity could be very different.

C. Comparison with measurements

During previous instability studies [18], macroparticle simulations were compared with dedicated measurements, where bunches with different intensities and approximately constant longitudinal emittance were injected into the SPS, accelerated following the cycle shown in Fig. 15, and were getting unstable above certain intensity. In general, the results of simulations through the ramp are very close to the observations if the latest impedance model is applied as shown in [22]. However, the instability mechanism was not yet proposed. Since the results of macroparticle simulations and numerical solutions of the linearized Vlasov equation agree for the parameters at the SPS flattop (Figs. 2 and 3), below we explore the mechanism of instabilities observed in the past measurements.

To understand the instability during the acceleration, we apply the eigenvalue analysis using matrix equations (29), which is implemented in the code MELODY. The main advantage of this approach is that we can obtain a snapshot of beam stability at any time during the cycle. In simulations, however, this is difficult since the energy changes every turn during acceleration, and only a very fast instability can be properly observed during the limited time of the small change in beam energy. Note that in the stability analysis, one also has to include the space-charge contribution to the total impedance model. At the injection energy of 26 GeV, the computed $\mathrm{Im}Z/k$ is about -1Ω [18], but it drops by an order of magnitude at 100 GeV and thus can be neglected at higher energies.

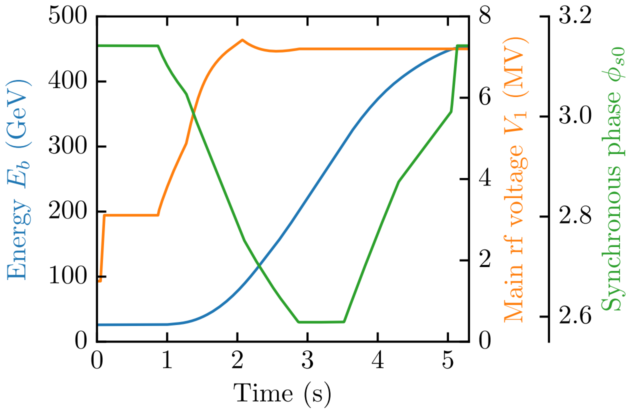

FIG. 15. The SPS acceleration cycle used during beam measurements [18]: beam energy (blue), main rf voltage (orange), and synchronous phase (green).

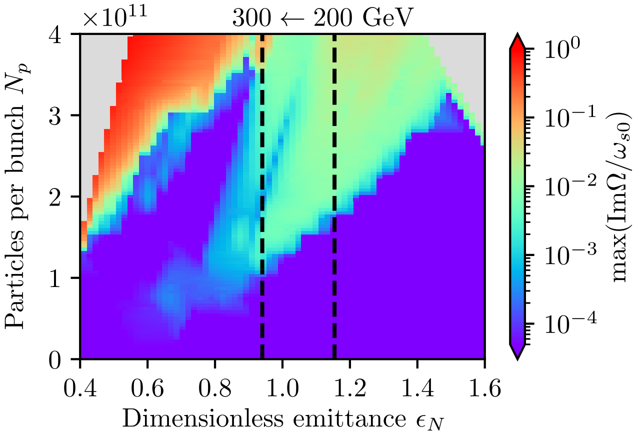

FIG. 16. Stability map applicable to various points of the acceleration (200–300 GeV) obtained with melody for $\phi_{s0} = 2.56$. Background color describes the instability growth rates. Two vertical dashed lines indicate the range of the dimensionless emittances for the total longitudinal emittance $\epsilon = 0.33$ eVs.

As was discussed in Sec. II A, the single-bunch stability for a given impedance model depends only on a few dimensionless parameters. In the single-rf case, these are ζ, ϵ_N, and ϕ_{s0}. Thanks to the systematic analysis performed by Gadioux [34], we have found that stability maps at intermediate energies through the cycle have similar non-monotonic behavior that the one at the flattop with the unstable "island." In Fig. 16, as an example, the map of bunch intensity versus the dimensionless emittance obtained from calculations with code MELODY is shown for $\phi_{s0} = 2.59$. It illustrates the beam stability during acceleration from 200 to 300 GeV since ϕ_{s0} and V_1 are constants (see Fig. 15). Since the dimensionless emittance ϵ_N reduces as energy increases for a given emittance ϵ [see, Eq. (8)], the bunch parameters move on the horizontal lines from right to left.

In Fig. 17, the measured data from [18] for bunch lengths and intensities after the arrival at the SPS flattop are presented. It includes the impact of the transfer function of the measurement system on the bunch profiles. Bunches with intensity below 1.2×10^{11} remain stable for the whole cycle. There is a "mild" instability in the intensity range 1.2–1.8×10^{11} already during the acceleration. Bunches with even higher intensities suffer from strong instability, which leads to uncontrolled longitudinal emittance blowup. The measured bunch length as a function of intensity approximately follows the line for the total longitudinal emittance of 0.33 eVs up to $N_p \approx 1.8 \times 10^{11}$ (red dashed line). For this emittance, the dimensionless emittance changes from 1.15 to 0.94 (the dashed lines in Fig. 16). Based on the stability map in Fig. 16, the bunches with an intensity of above 1.2×10^{11} will enter the unstable island

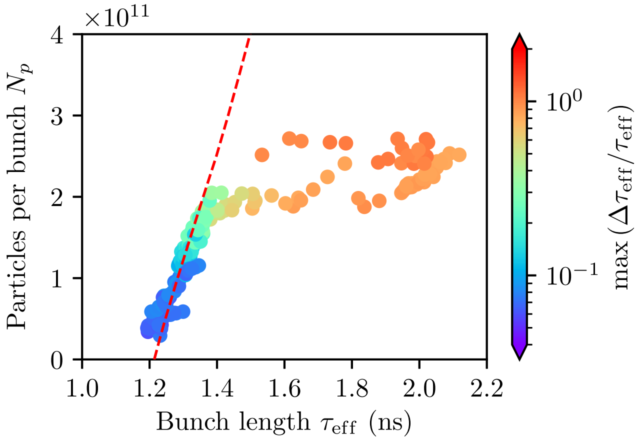

FIG. 17. The maximum oscillation amplitude of the bunch length during acceleration for different intensities and bunch lengths at the arrival at the SPS flattop obtained from measurements [18]. The red dashed line corresponds to computed bunch parameters with a constant emittance of $\epsilon = 0.33$ eVs.

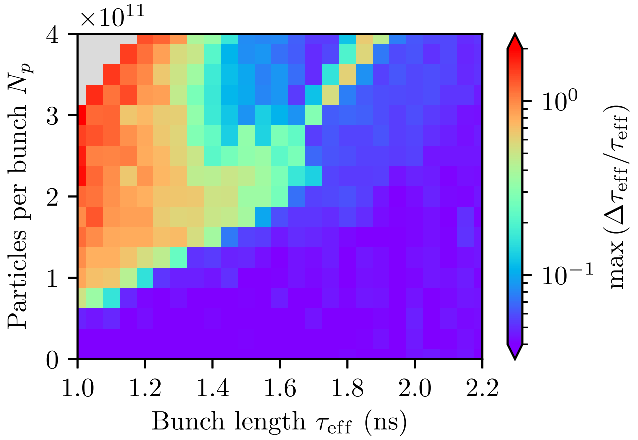

FIG. 18. Longitudinal stability map obtained from BLonD simulations for the SPS impedance model after LS2 (orange curve in Fig. 1) and single-rf configuration. Background colors indicate the maximum relative oscillation amplitude of the bunch length. The SPS parameters are according to Table I.

where the radial mode-coupling instability occurs. Depending on the time spent in that region, a fast enough instability will be able to develop. For even higher intensities, the bunches will become unstable even earlier in the ramp. Thus, we can conclude that the instabilities observed in the dedicated measurements during the ramp are indeed caused by the coupling of the radial modes.

IV. MITIGATION OF THE SPS INSTABILITIES

In this section, we discuss the ways applied to improve beam stability in the SPS. We saw above that the type of single-bunch instability and its threshold strongly depend on the synchrotron frequency distribution $\omega_s(\mathcal{E})$. This function can be significantly modified by the PWD, determined in turn by the SPS impedance model, and a HH rf system. The two stabilization methods based on this effect are used in the SPS and considered below.

A. Impact of the SPS impedance reduction

As an injector for the Large Hadron Collider (LHC), the SPS has been majorly upgraded during the last long shutdown (LS2) to be able to produce the multibunch beam required for the High Luminosity (HL)-LHC [35–37]. In particular, an impedance reduction campaign [37] has been performed, involving shielding of the specific type of vacuum flanges, 200 MHz rf system upgrade, and damping of its higher-order mode around 630 MHz by a factor of 3. A significant increase of instability thresholds for single-bunch and LHC-type beams in the double-rf system was expected from simulations and already observed for available intensities [38]. However, the stability of a single bunch in a single-rf configuration could be degraded for some bunch parameters [31]. Indeed, the top plot in Fig. 18 demonstrates that the stable region on the left-hand side of the unstable island now disappeared.

This effect can be again understood from the new shapes of $\omega_s(\mathcal{E})$ shown in Fig. 19. Bunches with an intensity of 2×10^{11} and a length of 1.3 ns were stable before impedance reduction because $\omega_s(\mathcal{E})$ was a monotonic function (blue). After LS2, an overlap of synchrotron frequencies for different $\mathcal{E}$ (orange) occurs, which results in the radial mode-coupling instability.

B. High-harmonic rf system

Double-rf operation in the SPS significantly increases the stability of all beams. The 800-MHz voltage is always applied in BSM, while there is no improvement of stability in BLM. The latter is practically limited by the extremely accurate programming of the relative phase Φ_4 in Eq. (4)

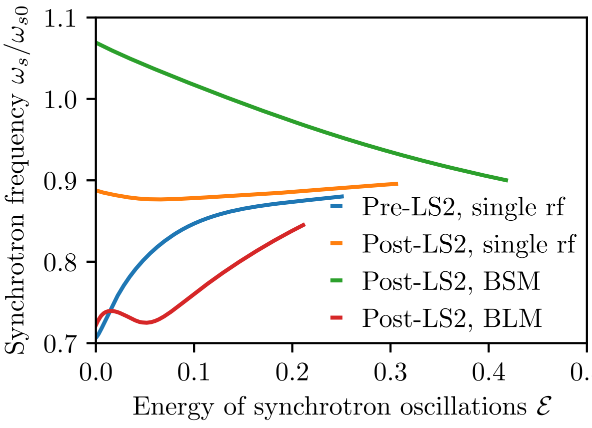

FIG. 19. Synchrotron frequency distributions for different impedance models and rf configurations at the intensity $N_p = 2\times 10^{11}$ and the bunch length $\tau_{\rm eff} = 1.3$ ns.

between the 200- and 800-MHz rf systems during the entire cycle [39]. Additionally, a strong PWD, especially due to the resistive part of the SPS impedance, also introduces a shift of the synchronous phase $\Delta\phi_s$, such that the relative phase Φ_4 computed without intensity effects is not optimal anymore. This leads to a nonmonotonic synchrotron frequency as a function of $\mathcal{E}$ (Fig. 19, red) and radial mode-coupling instability can occur. To suppress this instability for given bunch parameters, the relative phase Φ_4 must be precisely tuned to reestablish $\omega_s(\mathcal{E})$ as a monotonic function. If the intensity is very low, or the resistive impedance is negligible, the instability can be avoided, which is consistent with observations in another CERN synchrotron, the PS Booster (PSB) [40]. It is also known, that HH cavities operating in BLM allow raising the instability threshold of electron bunches (e.g., [13]). In particular, passive rf cavities can be used with a purely beam-induced rf voltage. To obtain a flat bunch profile, the amplitude and phase of the rf voltage are controlled by tuning the cavity center frequency. In this case, a weak radial mode-coupling instability due to nonmonotonic synchrotron frequency distribution is suppressed by the synchrotron radiation damping.

The operation in BSM is much less sensitive to the relative phase between rf systems and can help to suppress the harmful impact of PWD (Fig. 19, green). This rf configuration is routinely used in the SPS to deliver high-intensity bunches to the AWAKE experiment [41]. For example, for a voltage ratio of $r = 0.1$, there is a significant improvement in beam stability, in comparison to a single-rf case (Fig. 20). Typically, the instability threshold for short bunches gets higher for a larger ratio of rf voltages r, however, special attention is necessary for long bunches. These bunches may have a nonmonotonic synchrotron distribution for $r > 1/n$ and $n > 2$ even at zero intensity. The instability mechanism in this configuration is under study.

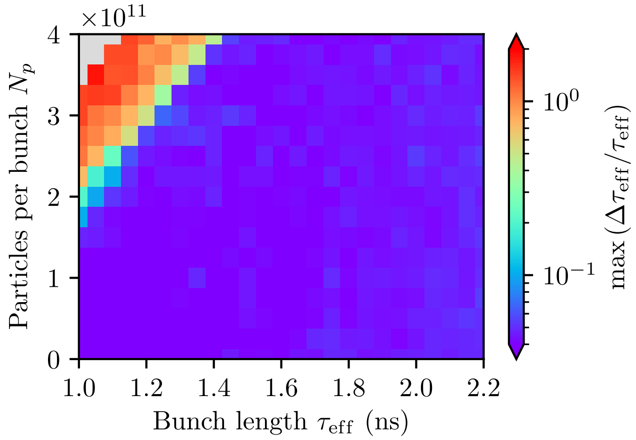

FIG. 20. Longitudinal stability map obtained from BLonD simulations for the SPS impedance model after LS2 (orange curve in Fig. 1) and double-rf configuration (BSM with a voltage ratio $r = 0.1$). Background colors indicate the maximum relative oscillation amplitude of the bunch length. The SPS parameters are from Table I.

V. CONCLUSION

We have demonstrated the existence of two different mechanisms of longitudinal single-bunch instability in the SPS: radial and azimuthal mode coupling. The results of fully self-consistent numerical calculations done using the code MELODY are able to explain all relevant observations in the SPS, including nonmonotonic dependence of thresholds on intensity and the presence of the unstable island. As this approach provides a snapshot of beam stability, the instability mechanism can be evaluated at any moment of the acceleration cycle. The predictions also agree well with the performed macroparticle simulations.

Previously, radial-mode coupling instability was obtained for very short, electron, bunches, when potential-well distortion plays an important role but rf nonlinearity can be neglected. We have shown that neglecting rf nonlinearity for long proton bunches leads to an underestimation of the real instability threshold up to a factor of 5. With intensity increase, radial mode coupling can appear simultaneously for several azimuthal modes and then has a signature of microwave instability.

Another instability type, azimuthal mode coupling, is also possible in the SPS, but for shorter bunches. In this case, the corresponding modes lose Landau damping (moving outside the incoherent frequency bands) and can become coupled above a certain beam intensity. This instability has a similar threshold but seems to be significantly weaker than the one obtained previously using non-self-consistent analysis (without PWD and rf nonlinearity). It can be suppressed by a small change in the particle distribution or even an increase in intensity. Additionally, we also observed a mixed mode-coupling instability, in which phase-space perturbation involves several azimuthal modes, and it has higher growth rates.

Longitudinal instabilities in the SPS are cured by operating in the bunch-shortening mode of the double-rf configuration, as it removes the nonmonotonic behavior of the synchrotron frequency as a function of synchrotron oscillation energy at the bunch center. Thus, for example, applying the fourth harmonic voltage at 10% of the main-rf voltage improves the stability of short bunches by almost a factor of 3, especially after the recent impedance reduction campaign. Longer bunches should be treated with caution due to the nonmonotonic behavior of synchrotron frequency distribution occurring with the fourth harmonic rf system.

ACKNOWLEDGMENTS

I wish to acknowledge Elena Shaposhnikova for fruitful discussions and valuable input to this manuscript. I am grateful to Heiko Damerau for his useful comments and continuous support. Special thanks also to Alexandre Lasheen, who provided the analyzed data from the dedicated experiments. Last but not least, I would like to thank Maxime Gadioux for his excellent work during the CERN Summer Student program 2020.

APPENDIX: AZIMUTHAL MODE-COUPLING INSTABILITY

The azimuthal mode-coupling instability mechanism was proposed by Sacherer in [1]. Here, we demonstrate that this is the only instability mechanism when rf nonlinearity and PWD are neglected. In this case, the functions I_{mk} according to Eq. (14) can be evaluated analytically. They become

$$I_{mk}(\mathcal{E}) = i^m J_m(k\sqrt{2\mathcal{E}}/h),$$

where $J_m(x)$ is the Bessel function of the first kind and the order m. Then, the nominator of the integrand of the spectral harmonics $\tilde{\lambda}_k(\Omega)$ from Eq. (23) becomes

$$\sum_{m=1}^{\infty} C_m(\mathcal{E},\Omega) I^*_{mk}(\mathcal{E}) = \sum_{p=1}^{\infty}(-1)^p \left\{ \mathrm{Re}[C_{2p}(\mathcal{E},\Omega)] J_{2p}\left(\frac{k}{h}\sqrt{2\mathcal{E}}\right) - \mathrm{Im}[C_{2p-1}(\mathcal{E},\Omega)] J_{2p-1}\left(\frac{k}{h}\sqrt{2\mathcal{E}}\right) \right\}$$
$$+ i \sum_{p=1}^{\infty}(-1)^p \left\{ \mathrm{Im}[C_{2p}(\mathcal{E},\Omega)] J_{2p}\left(\frac{k}{h}\sqrt{2\mathcal{E}}\right) + \mathrm{Re}[C_{2p-1}(\mathcal{E},\Omega)] J_{2p-1}\left(\frac{k}{h}\sqrt{2\mathcal{E}}\right) \right\}. \tag{A1}$$

Based on the Bessel function property for the integer argument $J_m(-x) = (-1)^m J_m(x)$, $|\tilde{\lambda}_k(\Omega)|^2$ is a symmetric function of k if either $\mathrm{Re}[C_m(\mathcal{E},\Omega)] = 0$ or $\mathrm{Im}[C_m(\mathcal{E},\Omega)] = 0$ for all azimuthal modes m. Thus, $\mathrm{Im}\Omega = 0$ according to Eq. (25), and the mode is stable. The instability requires that for at least one pair of azimuthal modes m and $m+1$, the eigenfunctions $\mathrm{Re}[C_m(\mathcal{E},\Omega)] \neq 0$ and $\mathrm{Im}[C_m(\mathcal{E},\Omega)] \neq 0$. Then, at least one element of the sum in the integrand is nonzero and $|\tilde{\lambda}_k(\Omega)|^2$ is asymmetric function of k, which is necessary condition for the instability. If only single azimuthal mode m has nonzero eigenfuctions $\mathrm{Re}[C_m(\mathcal{E},\Omega)]$ and $\mathrm{Im}[C_m(\mathcal{E},\Omega)]$, the symmetry of $|\tilde{\lambda}_k(\Omega)|^2$ is preserved and the bunch remains stable.

[1] F. J. Sacherer, Bunch lengthening and microwave instability, IEEE Trans. Nucl. Sci. **24**, 1393 (1977).

[2] G. Besnier, Stabilité des oscillations longitudinales d'un faisceau groupe se propageant dans une chambre a vide d'impedance reactive, Nucl. Instrum. Methods **164**, 235 (1979).

[3] J. M. Wang and C. Pellegrini, On the condition for a single bunch high frequency fast blow-up, in *Proceedings of 11th International Conference on High-Energy Accelerators, CERN, Geneva, Switzerland*, edited by W. S. Newman (Birkhäuser Basel, Basel, Switzerland, 1980), pp. 554–561.

[4] Y. H. Chin, K. Satoh, and K. Yokoya, Instability of a bunched beam with synchrotron frequency spread, Part. Accel. **13**, 45 (1983).

[5] S. Krinsky and J. M. Wang, Longitudinal instabilities with a non-harmonic rf potential, IEEE Trans. Nucl. Sci. **30**, 2492 (1983).

[6] J. L. Laclare, Bunched beam coherent instabilities, CERN, Geneva, Switzerland, Technical Report No. CERN-1987-003-V-1.264, 1987.

[7] J. P. Garnier, Instabilités cohérentes dans les accélérateurs circulaires, Ph.D. thesis, Institut National Polytechnique de Grenoble, Grenoble, France, 1987.

[8] K. Oide and K. Yokoya, Longitudinal single bunch instability in electron storage rings, KEK, Tsukuba, Japan, Technical Report No. KEK-Preprint-90-10, 1990.

[9] K. Oide, A mechanism of longitudinal single-bunch instability in storage rings, Part. Accel. **51**, 43 (1995).

[10] A. Chao, Bo Chen, and K. Oide, A weak microwave instability with potential well distortion and radial mode coupling, in *Proceedings of 16th Particle Accelerator Conference, Dallas, TX, 1995* (IEEE, New York, 1995), pp. 3040–3042.

[11] K. Y. Ng, Mode-coupling instability and bunch lengthening in proton machines, in *Proceedings of 16th Particle Accelerator Conference, Dallas, TX, 1995* (IEEE, New York, 1995), pp. 2977–2979.

[12] M. D'yachkov and R. Baartman, Longitudinal single bunch stability, Part. Accel. **50**, 105 (1995).

[13] A. Mosnier, Microwave instability in electron storage rings, Nucl. Instrum. Methods Phys. Res., Sect. A **438**, 225 (1999).

[14] Y. Cai, Linear theory of microwave instability in electron storage rings, Phys. Rev. ST Accel. Beams **14**, 061002 (2011).

[15] R. R. Lindberg, Practical theory to compute the microwave instability threshold, in *Nonlinear Dynamics and Collective Effects in Particle Beam Physics, Proceedings of NOCE 2017 Workshop, Arcidosso, Italy, 2017* (World Scientific, Singapore, 2019), pp. 138–146

[16] A. Blednykh, B. Bacha, G. Bassi, W. Cheng, O. Chubar, A. Derbenev, R. Lindberg, M. Rakitin, V. Smaluk, M. Zhernenkov, Y. K. Chen-Wiegart, and L. Wiegart, New aspects of longitudinal instabilities in electron storage rings, Sci. Rep. **8**, 11918 (2018).

[17] E. Métral and M. Migliorati, Longitudinal and transverse mode coupling instability: Vlasov solvers and tracking codes, Phys. Rev. Accel. Beams **23**, 071001 (2020).

[18] A. S. Lasheen, Beam measurements of the longitudinal impedance of the CERN Super Proton Synchrotron, Ph.D. thesis, Université Paris Saclay, Paris, 2017.

[19] A. Lasheen and E. Shaposhnikova, Evaluation of the CERN Super Proton Synchrotron longitudinal impedance from measurements of the quadrupole frequency shift, Phys. Rev. Accel. Beams **20**, 064401 (2017).

[20] CERN SPS Longitudinal Impedance Model, https://gitlab.cern.ch/longitudinal-impedance/SPS.

[21] CERN Beam Longitudinal Dynamics code BLonD, http://blond.web.cern.ch.

[22] J. Repond, Possible mitigations of longitudinal intensity limitations for HL-LHC beam in the CERN SPS, Ph.D. thesis, Ecole Politechnique, Lausanne, 2019.

[23] I. Karpov, Matrix Equations for LOngitudinal beam DYnamics (MELODY) code, https://gitlab.cern.ch/ikarpov/melody.

[24] A. Burov, Van Kampen modes for bunch longitudinal motion, in *Proceedings of 46th ICFA Advanced Beam Dynamics Workshop on High-Intensity and High-Brightness Hadron Beams, Morschach, Switzerland, 2010*, arXiv:1207.5826.

[25] A. W. Chao, *Physics of Collective Beam Instabilities in High Energy Accelerators* (Wiley, New York, 1993), Chap. 6, pp. 273–278.

[26] I. Karpov, T. Argyropoulos, and E. Shaposhnikova, Thresholds for loss of Landau damping in longitudinal plane, Phys. Rev. Accel. Beams **24**, 011002 (2021).

[27] N. G. Van Kampen, On the theory of stationary waves in plasmas, Physica (Utrecht) **21**, 949 (1955).

[28] N. G. Van Kampen, The dispersion equation for plasma waves, Physica (Utrecht) **23**, 641 (1957).

[29] K. M. Case, Plasma oscillations, Ann. Phys. (N.Y.) **7**, 349 (1959).

[30] M. Benedikt, P. Collier, V. Mertens, J. Poole, and K. Schindl, LHC design report Vol. 3: The LHC injector chain, CERN, Geneva, Switzerland, CERN Yellow Reports: Monographs, Report No. CERN-2004-003-V-3, 2004.

[31] E. Radvilas, Simulations of single-bunch instability on flat top, Technical Report No. CERN-STUDENTS-Note-2015-048, 2015.

[32] I. Karpov and M. Gadioux, Mechanism of longitudinal single-bunch instability in the CERN SPS, in *Proceedings of 12th International Particle Accelerator Conference, Campinas, SP, Brazil, 2021* (JACoW, Geneva, Switzerland, 2021), pp. 3161–3164.

[33] I. Karpov, T. Argyropoulos, S. Nese, and E. Shaposhnikova, New analytical criteria for loss of Landau Damping in longitudinal plane, in *Proceedings of 64th ICFA Advanced Beam Dynamics Workshop on High-Intensity and High-Brightness Hadron Beams, Batavia, IL, 2021* (JACoW, Geneva, Switzerland, 2022), pp. 100–105.

[34] M. Gadioux, Evaluation of longitudinal single-bunch stability in the SPS and bunch optimisation for AWAKE, CERN, Geneva, Switzerland, Technical Report No. CERN-STUDENTS-Note-2020-030, 2020.

[35] LHC Injectors Upgrade, Technical Design Report, Vol. I: Protons, edited by J. Coupard, H. Damerau, A. Funken, R. Garoby, S. Gilardoni, B. Goddard, K. Hanke, A. Lombardi, D. Manglunki, M. Meddahi, B. Mikulec, G. Rumolo, E. Shaposhnikova, and M. Vretenar, CERN, Geneva, Switzerland, Report No. CERN-ACC-2014-0337, 2014.

[36] E. Shaposhnikova, E. Ciapala, and E. Montesinos, Upgrade of the 200 MHz rf system in the CERN SPS, in *Proceedings of 2nd International Particle Accelerator Conference, San Sebastian, Spain, 2011* (JACoW, Geneva, Switzerland, 2011).

[37] E. Shaposhnikova, T. Argyropoulos, T. Bohl, P. Cruikshank, B. Goddard, T. Kaltenbacher, A. Lasheen, J. Perez Espinos, J. Repond, B. Salvant, and C. Vollinger, Removing known SPS intensity limitations for High Luminosity LHC goals, in *Proceedings of 7th International Particle Accelerator Conference, Busan, Korea, 2016* (JACoW, Geneva, Switzerland, 2016).

[38] V. Kain *et al.*, Achievements and performance prospects of the Upgraded LHC injectors, in *Proceedings of 13th International Particle Accelerator Conference, Bangkok, Thailand, 2022* (JACoW, Geneva, Switzerland, 2022), pp. 1610–1615.

[39] T. Bohl, T. P. R Linnecar, E. Shaposhnikova, and J. Tückmantel, Study of different operating modes of the 4th rf harmonic Landau damping system in the CERN SPS, CERN, Geneva, Switzerland, Technical Report No. CERN-SL-98-026-RF, 1998.

[40] S. C. P. Albright, F. Antoniou, F. Asvesta, H. Bartosik, C. Bracco, and E. Renner, New longitudinal beam production methods in the CERN Proton Synchrotron Booster, in *Proceedings of 12th International Particle Accelerator Conference, Campinas, SP, Brazil, 2021* (JACoW, Geneva, Switzerland, 2021), pp. 4130–4133.

[41] A. Caldwell, E. Adli, L. Amorim, R. Apsimon, T. Argyropoulos, R. Assmann, A.-M. Bachmann, F. Batsch, J. Bauche, V. K. Berglyd Olsen *et al.*, Path to AWAKE: Evolution of the concept, Nucl. Instrum. Methods Phys. Res., Sect. A **829**, 3 (2016).